Journal of Computational Applied Mechanics 2026, 57(3): 391-412

DOI: 10.22059/jcamech.2026.410596.1778

RESEARCH PAPER

Influence of Spanwise FGM and Numerical Parameters on the Fluid-Structure Interaction Response of a Cantilevered Plate Wing

M. S. Alzahrani [a], H. Qansh [a], Mohamed S. Abdelwahed [a], Mohamed A. Eltaher [a,b,*]

[a] *Department of Mechanical Engineering, Faculty of Engineering, King Abdulaziz University, Jeddah, Saudi Arabia*
[b] *Department of Mechanical Design and Production, Faculty of Engineering, Zagazig University, Egypt*

Abstract

This study investigates the nonlinear aeroelastic response and flutter behavior of a cantilevered plate wing using a two-way fluid–structure interaction framework in ANSYS, coupling Fluent and Mechanical. Both isotropic Aluminum and a spanwise functionally graded Al/Al_2O_3 material system are examined. The aerodynamic solver is validated against published S809 airfoil data, followed by validation of the cantilevered wing model. A sensitivity analysis is performed by varying the time step size (0.02–0.002 s) and the number of coupling iterations (5 and 10). Larger time steps introduce fluctuations in peak oscillation amplitudes and can delay growth through the critical flow speed window, whereas smaller time steps reduce these fluctuations and diminish iteration sensitivity. A mid-range configuration (Δt = 0.005 s, 10 iterations) provides results comparable to the finest settings at substantially lower computational cost. Using these parameters, the aeroelastic response of a spanwise functionally graded wing—constructed by dividing the span into ten segments with linear grading (k = 1)—is assessed. The FGM wing exhibits no flutter within the investigated flow speed range and shows markedly reduced tip displacement, maintaining RMS amplitudes below 0.01 mm, in contrast to the Aluminum baseline, which displays the expected increase in response with flow speed. The results demonstrate that a time step of 0.005 s with ten coupling iterations is sufficient for reliable flutter prediction under ANSYS student license constraints, and that spanwise FGM application significantly enhances aeroelastic stability.

Keywords: Vibration and Instability; Aeroelastic analysis; Flutter prediction; Fluid-structure interaction; Functionally Graded Material; Nonlinear Analysis; Finite volume and CFD.

1. Introduction

Aeroelasticity lies at the intersection of aerodynamics, elasticity, and structural dynamics, and it concerns the interaction between aerodynamic forces and structural deformation. flutter is the phenomena that can result from this

* Corresponding author M.A. Eltaher. Tel.: +966565518613, *E-mail address:* meltaher@kau.edu.sa, mohaeltaher@gmail.com

interaction. Flutter denotes a self excited dynamic instability driven by the interplay of aerodynamic, elastic, and inertial forces. In aerospace structures, this phenomenon is of particular concern because it can progress quickly and result in significant, potentially catastrophic, structural damage [1]. The nature of the field of Aeroelasticity is illustrated in a Venn diagram (Figure 1) which originated with Professor A. R. Collar in the 1940s [2].

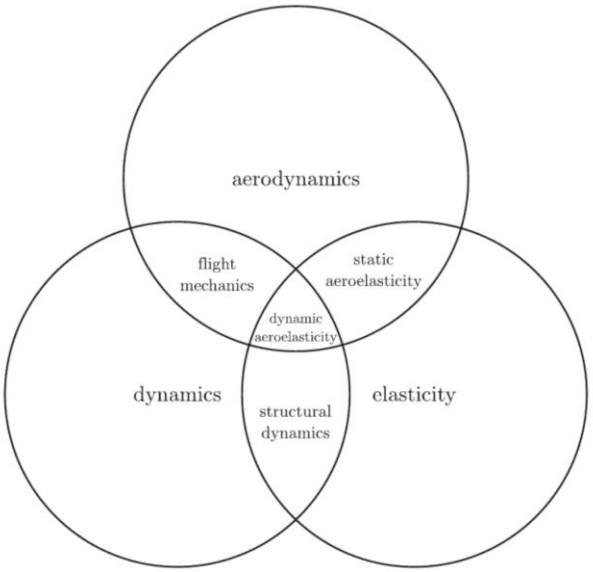

Figure 1: Venn diagram for the fields comprising aeroelasticity [2].

Due to the risk of developing an unstable vibration response induced by aeroelastic forces, aircraft manufacturers conduct extensive test flights to demonstrate that the aircraft is free of such vibrations within the operational specifications. With the development of more capable FEA software, the aircraft manufacturers first run various simulations to determine the stability of the design; this does not eliminate the need for test flights but contributes significantly to the reduction in cost. In this study, a specific wing design will be modelled and studied using FEA to determine the aeroelastic deformations and stability of the vibration response for different speeds.

Early coupled studies on AGARD 445.6 wing established the baseline for predictive aeroelastic simulation. Liu et al. [3] developed an integrated CFD-CSD framework and showed that flutter speed and frequency are well captured at subsonic and transonic speeds, with overprediction at supersonic conditions. Chen et al. [4] developed a fully coupled Navier-Stokes with a modal solver and again matched experiments across Mach 0.499 to 1.141. These studies show that the coupling strategy and aerodynamic fidelity become increasingly influential as compressibility effects increase, and that bias can be regime dependent. Bibin et al. [5] followed a pragmatic chain using multiple software: geometry in CATIA V5, meshing in ANSYS ICEM, aerodynamic loading from ANSYS Fluent, and then transferred to ANSYS Mechanical for stress/deformation analysis. Latif et al. [6] performed a semi-analytical 2D wing analysis using linear and torsional springs with an offset mass, and showed that flutter speed rises with spar thickness, while increasing the rib thickness decreases it; quantifying how local stiffness changes reshape stability margins. These works highlight accessible routes for design screening and clarify which structural parameters most leverage flutter boundaries.

Nonlinearity appears in several forms. Liu et al. [7] showed that the FG graphene nanoplatelets reinforced aluminum composite wing exhibits a growing disparity between linear and nonlinear models toward the tip, highlighting the need for nonlinear FSI. GUO et al. [8] examined multi-body morphing airfoils under steady and unsteady cases and found that skin flexibility can improve stability. Furquan & Mittal [9] pushed to fluid-membrane interaction with fracture using the element deletion method, demonstrating how hyperelastic membranes and failure criteria alter the coupled solution. For MAV-relevant membranes, Tiomkin & Raveh [10] found that compliant wings gain camber and lift at low AoA but are prone to luffing without pretension near-zero AoAs; regime maps governed by key nondimensional parameters such as mass ratio and Weber number, and accurate prediction requires resolving turbulent scales. These studies indicate that material and geometric nonlinearity are not optional details; they control both onset and post-onset responses.

Predicted flutter response can change noticeably even when the structural model is held constant, simply because the aerodynamic loads are evaluated and transferred differently. In an FSI framework, Valášek & Sváček [11] showed that the numerical choice of aerodynamic forces calculations can lead to different responses by comparing three alternative force-computation approaches. The related work of Sváček [12] on control-surface-coupled

configuration shows that actuation coupling can shift the flutter speed. On the experimental side, faster validation loops are becoming more feasible. Transonic flutter wind-tunnel models manufactured using metal additive manufacturing (AlSi10Mg) were shown to achieve adequate surface quality and internal geometric accuracy, reducing both cost and lead time and supporting more rapid compute-test iteration [13]. Liu and Ma [14] modeled the fully unfolded axially moving wing as a stepped cantilever plate, examines the system's structural nonlinearities, and investigated how aerodynamic nonlinearities affect their vibrational response. Abdoulaye and Maani [15] presented a numerical study of fluid–structure interaction (FSI) applied to wind turbines, combining CFD and FEA. Knight et al. [16] presented FSI of symmetrical and cambered spring-mounted wings using various spring preloads and pivot point locations. Hadebe et al. [17] presented an integrated structural–hydraulic optimization of a DN3000 Boving butterfly valve blade rated for a maximum operating pressure of 10 bar with comparative analysis of a conventional flat blade and an optimized curved blade.

In extreme flight regimes, aeroelastic stability is often shaped by physics that are negligible at lower speeds. For hypersonic-relevant configurations, Wang et al. [18] incorporated thermal-fluid-structure coupling, which has shown to shift the flutter boundary, indicating that heating and related multi-physics effects can alter predicted margins. Interaction effects become equally important when lifting surfaces operate in close proximity. In biplane arrangements, reducing the gap between wings lowers flutter speed, with backward sweep further decreasing stability margins; by contrast, stagger can be beneficial at small gaps, while dihedral appears to have a comparatively minor influence, according to Dhital et al. [19]. The resulting motion commonly evolves toward out-of-phase behavior, and LCO may occur beyond the critical speed, supporting a design-relevant interpretation: closely spaced wings may be treated as a single coupled aeroelastic system, with gap, sweep, and stagger acting as primary drivers. Guo et al. [20] addressed the issues of nonlinear and thermal-coupled vibration control within the context of space-based flexible solar panel systems.

In rotating systems, aeroelastic constraints are tightly coupled to performance objectives and to uncertainty in the structural dynamics. The multi-objective design workflow that combines free-form deformation with Kriging surrogates and a genetic algorithm, presented by Fan et al. [21] has shown to improve compressor/rotor performance while reducing forced-response sensitivity under frequency mistuning, yielding gains in total pressure and efficiency alongside reduced amplitude magnification; the data-mining results point to a practical compromise: increasing blade twist was reported to correlate negatively with aerodynamic damping, highlighting a recurring performance-stability trade-off in turbomachinery design. Zhang et al. [22] examined nonlinear transient response of graphene platelets reinforced metal foams annular plate considering rotating motion and initial geometric imperfection. Li et al. [23] studied shear lag effect of ultra-wide box girder under influence of shear deformation.

For wind turbines, the dominant issue is often whether the model captures the coupled physics that drive fatigue-relevant loads. Using two-way FSI with LES and an 8 DoFs blades-tower structural representation, turbulence was shown to significantly increase response variability and equivalent fatigue loads, with flap-wise blade motion contributing most strongly; including tower flexibility can also redistribute energy and damp selected components of the response [24]. Similar conclusions emerge from time-variant two-way coupling frameworks that pair BEM theory with hybrid beam structural models and modified Newmark-β time integration, where agreement with GH Bladed/NREL 5-MW trends was reported (maximum difference is 3.13%) and out-of-plane deformation was found to strongly influence aerodynamic load and dynamic response caused by aeroelastic coupling [25]. In combination, these results reinforce that one-way coupling or reduced structural degrees of freedom may miss interactions that are essential to fatigue assessment and control-oriented design. Frulla and Parente [26] presented and discussed design considerations for a compressed stiffened plate with skin–stringer debonding based on the evaluation of adhesive layer stress distribution. Mahmoudi et al. [27] investigated dynamics behavior and stability of axially functionally graded fluid-conveying nanotube including solid fluid interaction. Kherief [28] examined numerical simulation of laminar flow of a non-newtonian bentonite solution in a horizontal pipe.

In this study, a specific wing design will be modelled and studied using FEA to determine the aeroelastic deformations and stability of the vibration response for different speeds. This study has two goals. First, the numerical settings are studied, specifically how the time step (Δt) and the number of fluid-solid coupling iterations in an ANSYS Fluent-Mechanical workflow, affect the predicted flutter onset for a flat-plate wing, providing practical guidance on accuracy-cost trade-offs for reproducible aeroelastic simulations. Second, a single functionally graded material (FGM) design is evaluated (spanwise grading) against a homogeneous Aluminum baseline to determine whether spanwise grading alone shifts the flutter boundary under identical modelling assumptions. Thus, isolating the sensitivity of flutter onset to solver controls, and the aeroelastic benefit (or lack thereof) of this specific FGM implementation relative to metal. The literature rarely addresses the practical constraints of free commercial software for a two-way FSI framework; thus, the present work aims to fill this gap by recommending suitable numerical settings. Additionally, the like-for-like comparison of the spanwise FGM and baseline model isolates the effect of material distribution on flutter in the subsonic regime.

This paper is organized as follows. Section **Error! Reference source not found.** shows the governing equations for CFD and FEA. Section **Error! Reference source not found.** starts by validating the CFD solver, then presents the FSI model, and its validation against the literature. Section **Error! Reference source not found.** shows the effects of numerical settings (time-step size and coupling iterations) and spanwise FGM on flutter behaviour. Section **Error! Reference source not found.** gives a summary of the main conclusions of the study.

2. Formulation and finite element model

The nature of the flutter behavior can be quite complex to simulate, since it is a flexible body response to fluid movement, thus requiring Multiphysics (fluid-structure) interactions to simulate. ANSYS Mechanical and ANSYS FLUENT were coupled through the System Coupling module within ANSYS Workbench as a black box process, to simulate the transient response of the flexible body to aerodynamic forces. The simple cantilever wing examined by Dhital et al. [19] will be used in this study.

2.1. CFD governing equations

The turbulence model used is the SST k-ω,

$u = U + u'$ (1) is substituted in Navier-Stokes equations.

$$u = U + u' \tag{1}$$

Where: u is the turbulence velocity, U is turbulence averaged velocity, and u' is the turbulence fluctuation velocity. By substituting

$u = U + u'$ (1) into Navier-Stokes equations, the Reynold's Averaged Navier-Stokes Equation is obtained [29]:

$$\rho\left(\frac{\partial U_i}{\partial t} + U_j\frac{\partial U_i}{\partial x_j}\right) = \frac{\partial p}{\partial x_i} + \frac{\partial}{\partial x_j}\left(\mu\frac{\partial U_i}{\partial x_j} - \rho\overline{u_i' u_j'}\right) \tag{2}$$

Where: U_i is the averaged air velocity components $\left(U_x, U_y, U_z\right)$, x_j is coordinate system (x, y, z), t is the time, μ is the air dynamic viscosity, and $\overline{u_i' u_j'}$ is Reynolds turbulent stress. The $SST\ k-\omega$ turbulent model is introduced by Menter [30] Eq (3) and (4):

$$\frac{\partial}{\partial t}(\rho k) + \frac{\partial}{\partial x_i}(\rho k u_i) = \frac{\partial}{\partial x_j}\left(\Gamma_k\frac{\partial k}{\partial x_j}\right) + \tilde{G}_k - Y_k \tag{3}$$

$$\frac{\partial}{\partial t}(\rho\omega) + \frac{\partial}{\partial x_i}(\rho\omega u_i) = \frac{\partial}{\partial x_j}\left(\Gamma_\omega\frac{\partial \omega}{\partial x_j}\right) + G_\omega - Y_\omega + D_\omega \tag{4}$$

2.2. Where: Γ_k is the effective diffusivity of k, $\tilde{G}_k$ is the generation of turbulence kinetic energy due to mean velocity gradients, Y_k is dissipation of k, ω is specific dissipation rate, Γ_ω is effective diffusivity of ω, G_ω is generation of ω, Y_ω is dissipation of ω, D_ω is a cross-diffusion term.

2.3. FEA governing equations

In finite element analysis of continuous systems, the equilibrium equation is [31, 32]:

$$M\ddot{U} + C\dot{U} + KU = R \tag{5}$$

Where M is the mass matrix, C is the damping matrix, K is the stiffness matrix, U is displacement vector (the dots denote time derivative), and R is the force vector. For time marching, the Newmark-β [33] method is employed, which is unconditionally stable for systems at $\gamma = \frac{1}{2}$ and $\beta = \frac{1}{4}$, these two parameters were introduced by Newmark to indicate how much the acceleration affects the relations of velocity and displacement.

$$ {}^{t+\Delta t}\dot{U} = {}^{t}\dot{U} + \left[\left(1-\gamma\right) {}^{t}\ddot{U} + \gamma \, {}^{t+\Delta t}\ddot{U} \right] \Delta t \tag{6} $$

$$ {}^{t+\Delta t}U = {}^{t}U + {}^{t}\dot{U}\Delta t + \left[\left(\frac{1}{2} - \beta \right) {}^{t}\ddot{U} + \beta \, {}^{t+\Delta t}\ddot{U} \right] \Delta t^2 \tag{7} $$

For the solution of displacements, velocities, and accelerations at $t + \Delta t$, **Error! Reference source not found.**) becomes:

$$ M \, {}^{t+\Delta t}\ddot{U} + C \, {}^{t+\Delta t}\dot{U} + K \, {}^{t+\Delta t}U = {}^{t+\Delta t}R \tag{8} $$

By re-arranging Eq. **Error! Reference source not found.**) to solve for ${}^{t+\Delta t}\ddot{U}$, then substituting into Eq. ${}^{t+\Delta t}U = {}^{t}U + {}^{t}\dot{U}\Delta t + \left[\left(\frac{1}{2} - \beta \right) {}^{t}\ddot{U} + \beta \, {}^{t+\Delta t}\ddot{U} \right] \Delta t^2$ (7), equations for ${}^{t+\Delta t}\ddot{U}$ and ${}^{t+\Delta t}\dot{U}$ in terms of ${}^{t+\Delta t}U$ only are obtained. These two equations can then be substituted into Eq. $M \, {}^{t+\Delta t}\ddot{U} + C \, {}^{t+\Delta t}\dot{U} + K \, {}^{t+\Delta t}U = {}^{t+\Delta t}R$ (8) to solve for the unknown displacement ${}^{t+\Delta t}U$. After that, ${}^{t+\Delta t}\ddot{U}$ and ${}^{t+\Delta t}\dot{U}$ can be calculated [33].

2.4. Fluid-Solid Interaction model

The simple cantilevered wing is used in this study of the flutter behavior. Dhital et al. [19] simulated the flutter response of a rectangular cantilevered wing having a 2.5 aspect ratio and the properties in Table 1:

Table 1: Properties of the wing model

Property	Value	unit
Chord length (c)	0.425	m
Thickness	0.002	m
Density	2700	kg/m^3
Poisson's ratio	0.3	
Young's modulus	70	GPa

Arrondeau & Rana [34] published a paper about multi-element wings in ground effect, they searched the literature for an appropriate domain size. The domain was broken down into a few parameters (dimensions): L_u is the upstream length, L_d is the downstream length, L_c is the crosswise (spanwise) length, and H is the height. Based on the literature (eight published scientific papers), Arrondeau & Rana elected the domain size to be $L_u = 8c$, $L_d = 15c$, $L_c = 10c$, and $H = 9c$ (c is the chord length). A large enough domain size ensures minimal interference from the domain boundaries on the fluid flow near the wing, allow the upstream flow to fully develop, and capture wake and vortex shedding. Due to software license limitations, the domain size is limited to $L_u = 1.18c$, $L_d = 4.71c$, $L_c = 4.71c$, and $H = 2.82c$ (Figure 2).

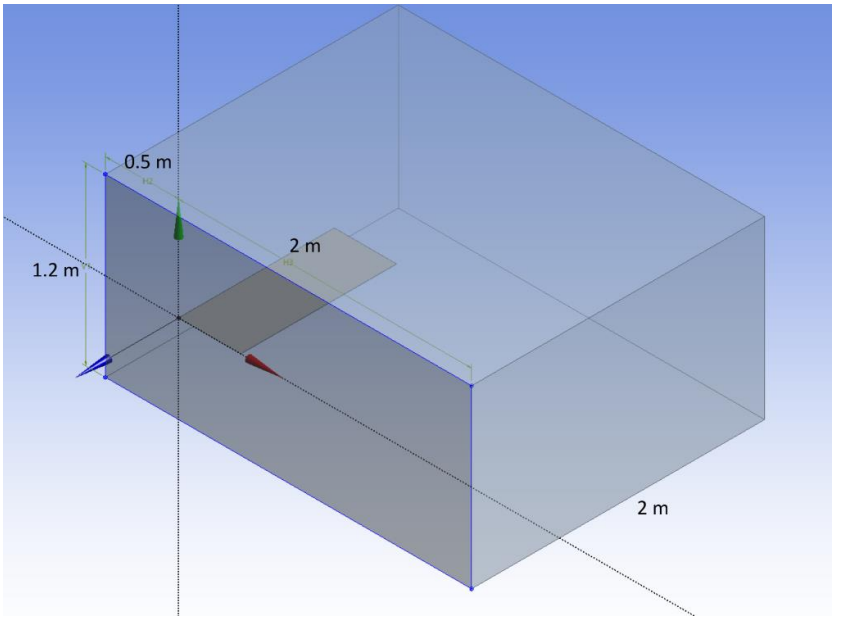

Figure 2: Fluid domain dimensions

This simulation will be performed using the System Coupling module in ANSYS, where FLUENT will solve for one time step, and get the aerodynamic forces on the wing boundary. These forces will then be transferred to the wing in Mechanical and solved for the wing deformation. This deformation will be transferred back to FLUENT to update the mesh and proceed to the next time step. For this to work, the models must be set up in a specific way in their respective programs. Figure 3 shows the setup in FLUENT, the boundary conditions setup as a no-slip wall for the wing boundary surfaces, inlet surface as a velocity inlet, outlet surface as a pressure outlet, and symmetry for all other domain surfaces.

Since the simulation is performed to capture the flutter onset, the air velocity is not constant; therefore, a user-defined function for the inlet air velocity is used. Following the work of Dhital et al. [19], the airflow starts at 25 m/s for the first two seconds, then 25.6 m/s for another two seconds (critical speed), then 26.35 m/s for four seconds, after that the airflow velocity keeps increasing by 1 m/s every four seconds until the simulation ends at 20 seconds. The maximum inlet airflow velocity is 29.35 m/s, equivalent to Mach 0.08552 for air at sea level; for such a low Mach number, essentially below Mach 0.3, air can be considered incompressible Oosthuizen & Carscallen [35]. By ignoring compressibility, computational cost is reduced.

The wing is modeled in ANSYS Mechanical as a plate of 0.002 m thickness, 0.425 m chord, and 1.0625 m span. The root of the wing is set as a fixed support, and all the other surfaces are set for the coupled analysis. Figure 4 shows the boundary conditions applied in ANSYS Mechanical. Once the individual programs are set up, they are linked using System Coupling (Figure 5).

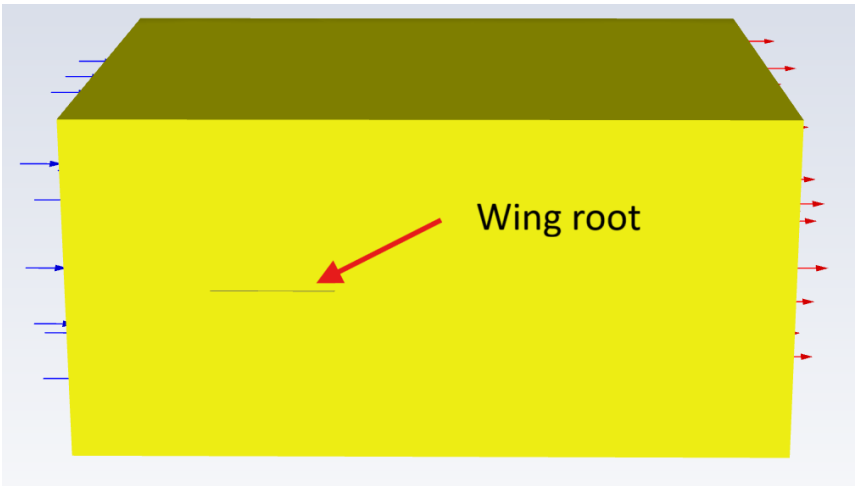

Figure 3: Fluid domain

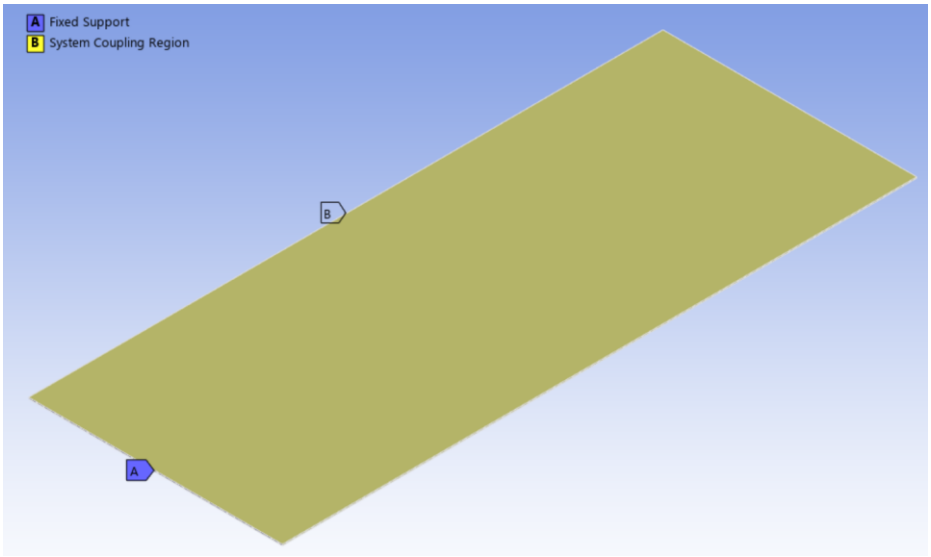

Figure 4: Wing model in ANSYS Mechanical.

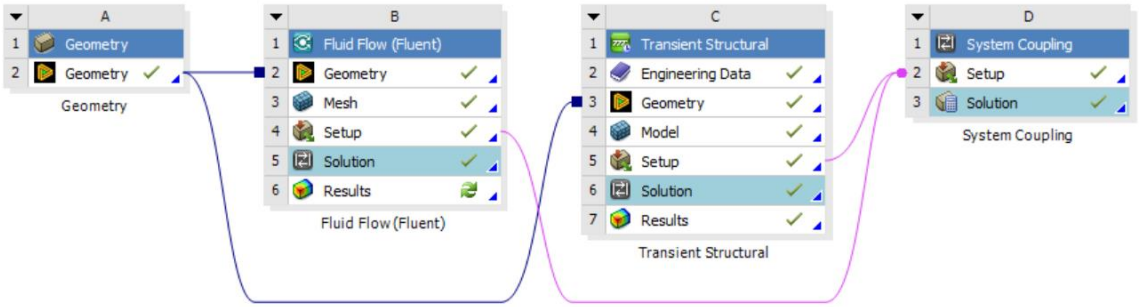

Figure 5: System Coupling scheme

The coupled transient solution was executed in ANSYS System Coupling using RMS-based convergence monitoring of the transferred quantities. Convergence of each coupling step is evaluated at the end of every coupling iteration and requires that the target-side RMS change of the transferred data reaches the prescribed convergence criterion, and that the specified minimum number of coupling iterations is satisfied; otherwise, additional coupling iterations are performed. In the present setup, the data-transfer convergence target was set to 0.01 (RMS-based. Since each additional coupling iteration triggers further exchanges and solver updates within the same physical time step, increasing the iterations per step directly increases computational cost, which motivated limiting the parametric study to 5 and 10 coupling iterations.

3. Validation

This section presents the validation steps that were carried out before conducting the parametric studies. The objective is to ensure that the aerodynamic solver reproduces published and experimental trends, and that the coupled FSI setup can predict a reference flutter response reported in the literature. The validation is therefore performed in two stages: first, the CFD solver is verified using the S809 airfoil force coefficients, and then the complete FSI model of the cantilevered plate wing is validated against a published aeroelastic case.

3.1. Validation of the aerodynamic solver

Qansh [36] Study Case 2 examined the 2D force coefficients of S809 airfoil using two different turbulence models, Spalart-Allmaras (S-A) model and SST k-ω model. Then compared the results with S-A results published by Xu et al. [37], and validated using wind tunnel experiments conducted by Butterfield et al. [38]. The geometry selected by Qansh [36] was based on the wind tunnel experimental data, where the fluid domain was 3.66 m high by 25.83 m wide, airfoil chord length of 0.457 m, and placed 12.8 m from the velocity inlet.

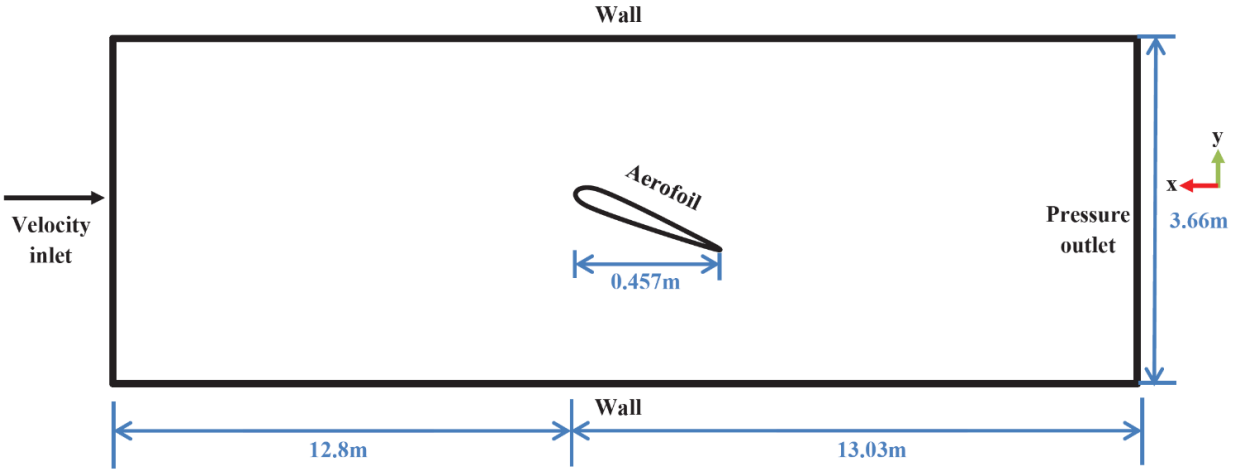

Figure 6: Illustration of the setup by Qansh (2022)

This study will be used to validate the aerodynamic model, varying the angle of attack of an S809 airfoil from 0° to 20° with an increment of 4°. The wind velocity is 26 m/s, and the turbulence model used is SST k-ω. Figure 7 shows the lift coefficient compared to Butterfield et al. [38] experimental results, Xu et al. [37] S-A simulation, and Qansh [36] simulations. The results of the current simulation are almost identical to the two-equation model by Qansh [36], which makes sense as the same turbulence model is used here. Figure 8 shows the drag coefficient compared to the previously published work. Both figures show the superiority of the SST k-ω (two-equation) turbulence model over Spalart-Allmaras' results, as it agrees better with the experimental results. This is clearly shown at AoA larger than 16° (stall condition).

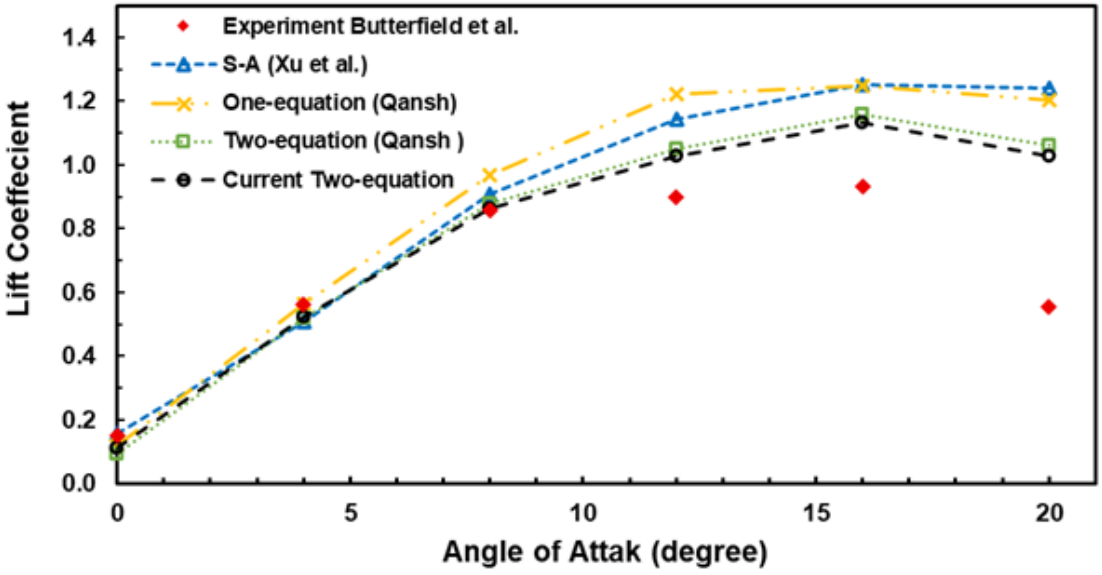

Figure 7: Lift coefficient of 2D S809 airfoil.

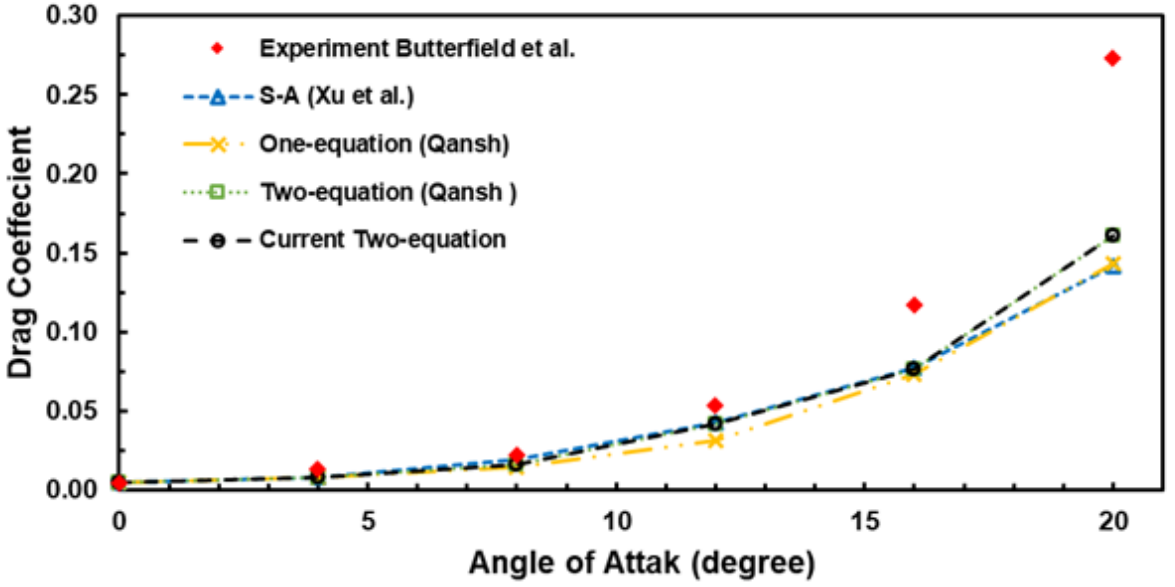

Figure 8: Drag coefficient of 2D S809 airfoil

3.2. Validation of the FSI model

The time step size and number of iterations in the simulation by Dhital et al. [19] were not clearly provided in the literature and were therefore assumed to be 0.01 seconds and five iterations. Figure 9 shows the results reported by Dhital et al. [19].

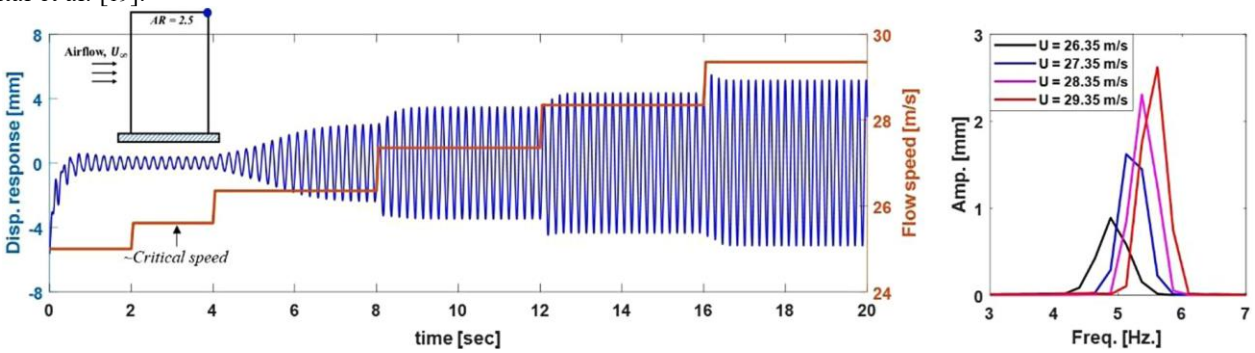

Figure 9: Trailing edge tip response reported by Dhital et al. [19]

The simulation's total runtime is 20 hours. Figure 10 shows the time history displacement response at the tip of the wing's trailing-edge. The Fast-Fourier Transform (FFT) is applied to the displacement data to obtain the frequencies. The flutter onset speed and dominant flutter frequencies are in good agreement with Dhital et al. [19]; however, the present FSI model predicts a larger LCO plateau amplitude (around 30 mm at air speed 29.35 m/s) than reported by Dhital et al. [19] (~5 mm). This difference can be attributed primarily to differences in numerical resolution and computational domain size. The mesh-count constraints in the current work limit the spatial resolution of the near-surface/interface region and wake development, which can affect the predicted aerodynamic. Likewise, the reduced domain may alter the unsteady load environment through boundary-condition influence. In addition, the structural model in the present study was implemented without structural damping, which reduces physical dissipation and can increase the amplitude in the post-critical regime. Dhital et al. do not explicitly state whether structural damping was included in their structural formulation; thus, differences in dissipation modelling between the two studies cannot be excluded.

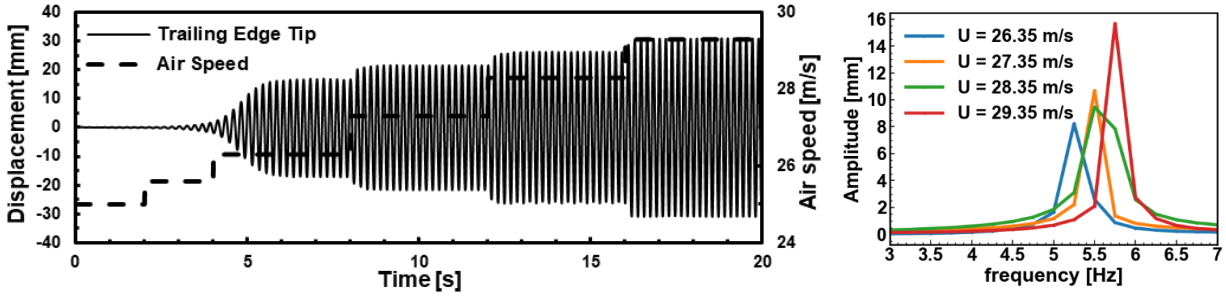

Figure 10: Trailing edge tip response

4. Results and discussion

The validated baseline is used to examine the model's numerical sensitivity to the chosen time step size and the number of iterations per time step, and to determine how these parameters influence the predicted flutter onset, dominant frequency, and steady-state response amplitude. Following that, the spanwise functionally graded material (FGM) case is studied against the baseline, outlining its intended role in reshaping mass-stiffness distribution.

4.1. Effect of time step and number of iterations

After the validation of the FSI model, the effects of the assumed parameters (time step size and number of iterations) are studied. Due to the high computational cost, the simulations are limited to a manageable number; time step sizes of 0.02, 0.01, 0.005, and 0.002 seconds are considered. For each step size, five and ten iterations will be studied, giving a total of eight simulations to study the assumed parameters. The eight simulations were conducted under identical conditions, varying only the time step size and the number of iterations. For each interval of air speed above the critical, the response develops into limit-cycle oscillations (LCO), where the peaks of the tip displacement plateau. The LCO characteristics are analyzed to obtain quantifiable parameters for comparisons. First, the plateau amplitude is computed, using the Hilbert transform to obtain the envelope of the tip response, then finding the envelope's median value over a specified region of the segment (air speed interval). Second, the detection of LCO is defined as the time at which the envelope remains within a prescribed tolerance band around its subsequent plateau value for a sustained duration; this is used to find the time-to-LCO, which is the time when the first LCO is detected in the entire run. Figure 11 shows the LCO analysis of the validation run. In addition, the coefficient of variation (CV) of the plateau peak displacements was used to quantify cycle-to-cycle peak fluctuations that are visually apparent in some cases, by calculating the CV for each LCO plateau, then finding the mean for all LCO plateaus of the run. The same segmentation and extraction procedure is applied to all eight simulations, ensuring that observed differences in LCO onset and steady amplitude are attributed to the selected time-step size and the number of coupling iterations. Table 2 is a summary of the LCO analysis results for each simulation, and Table 3 shows the dominant frequency for each air speed above critical.

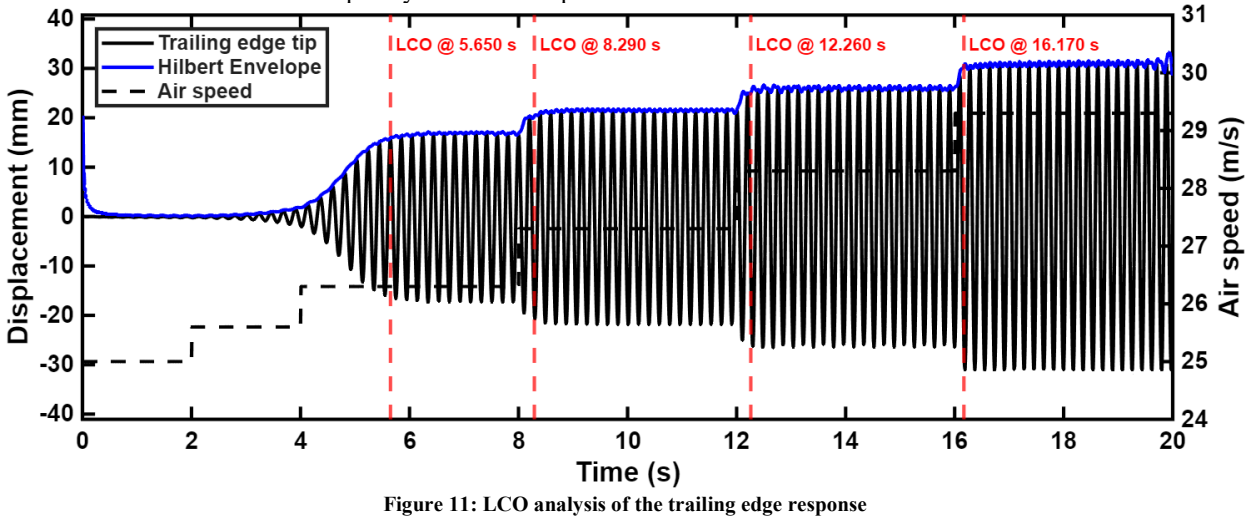

Figure 11: LCO analysis of the trailing edge response

Table 2: Time step and iteration study

Simulation	Time step	Iterations	Time-to-	Amp of First	Mean CV	Total run time [days]

	[s]	per step	LCO [s]	LCO [mm]		
1	0.02	5	8.52	19.35	0.028972	0.40
2	0.02	10	5.36	18.11	0.015752	0.75
3[†]	0.01	5	5.65	16.93	0.007801	0.85
4	0.01	10	5.55	19.31	0.008828	2.1
5	0.005	5	5.11	17.82	0.004786	1.6
6	0.005	10	4.53	18.21	0.004539	3.0
7	0.002	5	4.778	18.38	0.007157	3.9
8	0.002	10	4.718	18.37	0.005037	7.5

Table 3: Dominant frequencies (Hz) of air speeds above the critical

Simulation	Dominant freq at V3	Dominant freq at V4	Dominant freq at V5	Dominant freq at V6
1	4.5	5	5	5.25
2	5	5	5.25	5.5
3	5	5.25	5.5	5.5
4	5.25	5.5	5.75	5.75
5	5.25	5.5	5.5	5.75
6	5.25	5.5	5.5	5.75
7	5.25	5.5	5.75	5.75
8	5.25	5.5	5.75	5.75

Figure 12 through Figure 19 show the results of the eight simulations. At the largest time step ($\Delta t = 0.02$ s), noticeable cycle-to-cycle peak fluctuation is observed, which is consistent with the highest CV values, particularly near the lower supercritical velocity steps. Simulation 1 ($\Delta t = 0.02$ s, 5 iterations) shows the largest mean CV (0.02897) and the most severe irregularity in the plateau peaks. This is reflected also in the transient behaviour: the time-to-LCO is substantially delayed (8.52 s) well after the critical speed, indicating that the solution does not transition to the LCO in a timely manner relative to the velocity schedule. Increasing the number of iterations at the same time step (Simulation 2) improves the response onset behavior, reducing the time-to-LCO to 5.36 s and decreasing the mean CV to 0.01575; however, the plateau remains comparatively scattered, and the dominant frequencies increase across the supercritical velocities (e.g., V6 increases from 5.25 to 5.5 Hz). This behavior supports that, under coarse Δt, more coupling iterations can reduce the delay of time-to-LCO but may also affect both the frequency estimate and the cycle-to-cycle peak consistency.

For $\Delta t = 0.01$ s (Simulations 3 and 4), the response becomes more stable than the $\Delta t = 0.02$ s cases, but peak variations are still present at the higher velocities. The mean CV values (0.00780 for Simulation 3 and 0.00883 for Simulation 4) indicate that peak fluctuation is substantially reduced compared with $\Delta t = 0.02$ s, yet remains above the best-performing cases. The time-to-LCO is also consistent between the two runs (5.65 s and 5.55 s), suggesting that the transient-to-LCO evolution is captured more reliably at this time step. The dominant frequencies, however, exhibit a systematic shift with iterations: at the supercritical steps, Simulation 4 (10 iterations) produces consistently higher dominant frequencies than Simulation 3 (5 iterations), reaching 5.75 Hz at V5 and V6. This indicates that, at $\Delta t = 0.01$ s, the iteration count still influences the aeroelastic response, even though the transient settling times are similar.

At $\Delta t = 0.005$ s (Simulations 5 and 6), the agreement between runs improves markedly and the plateau behavior becomes the most consistent of all tested time steps. Both simulations predict similar frequency content and show the same dominant frequencies at each supercritical velocity (V3 = 5.25 Hz, V4 = 5.5 Hz, V5 = 5.5 Hz, V6 = 5.75 Hz). The CV results confirm the visual observation of reduced peak fluctuation: the mean CV falls to 0.00479 (5

[†] Simulation 3 is the validation simulation presented in Figure 10

iterations) and 0.00454 (10 iterations), representing the lowest overall fluctuation levels across the study. Additionally, the time-to-LCO is reduced relative to larger Δt (5.11 s and 4.53 s). These results suggest that Δt = 0.005 s is sufficiently small to capture the oscillation details without introducing the pronounced cycle-to-cycle irregularities seen at Δt = 0.02 s, and without materially altering the plateau amplitude.

For the smallest time step (Δt = 0.002 s; Simulations 7 and 8), the responses are very similar in both the time and frequency domains: the dominant frequencies at each supercritical step are identical for both iteration counts (V3 = 5.25 Hz, V4 = 5.5 Hz, V5 = 5.75 Hz, V6 = 5.75 Hz), and the first-LCO plateau amplitudes are essentially unchanged (18.38 and 18.37 mm). The mean CV values are low (0.00716 for 5 iterations and 0.00504 for 10 iterations), confirming that plateau peak scatter is limited; however, these values do not improve upon the Δt = 0.005 s cases, and the computational cost increases substantially. In particular, Simulation 8 requires the longest runtime (7.5 days), despite producing frequency and amplitude results that are not meaningfully different from those obtained at Δt = 0.005 s.

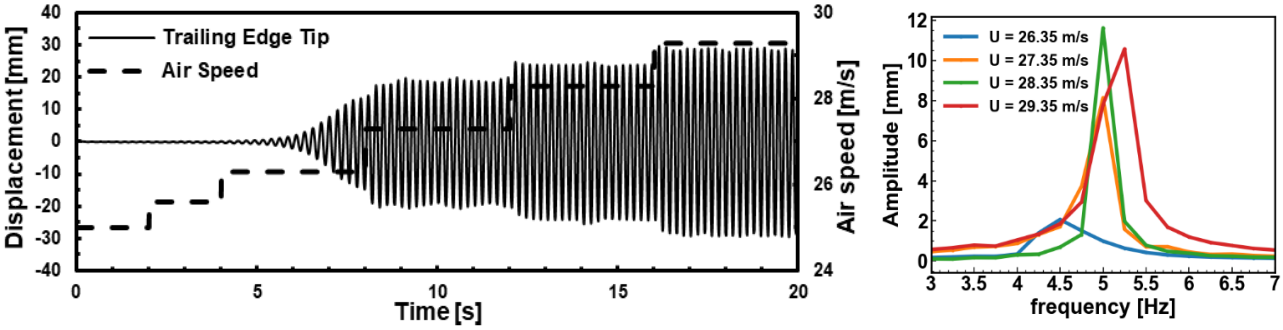

Figure 12: Simulation 1, step size 0.02 [s] and 5 iterations

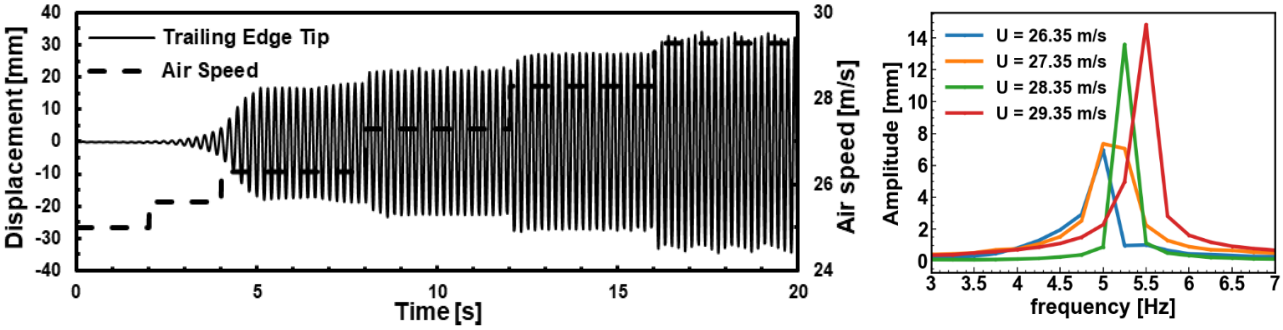

Figure 13: Simulation 2, step size 0.02 [s] and 10 iterations

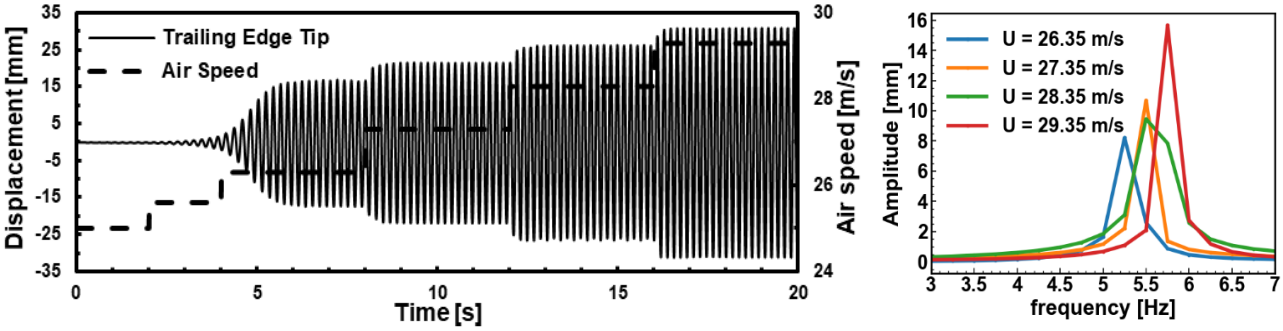

Figure 14: Simulation 3, step size 0.01 [s] and 5 iterations (repeated Figure 10 to ease the comparison for readers)

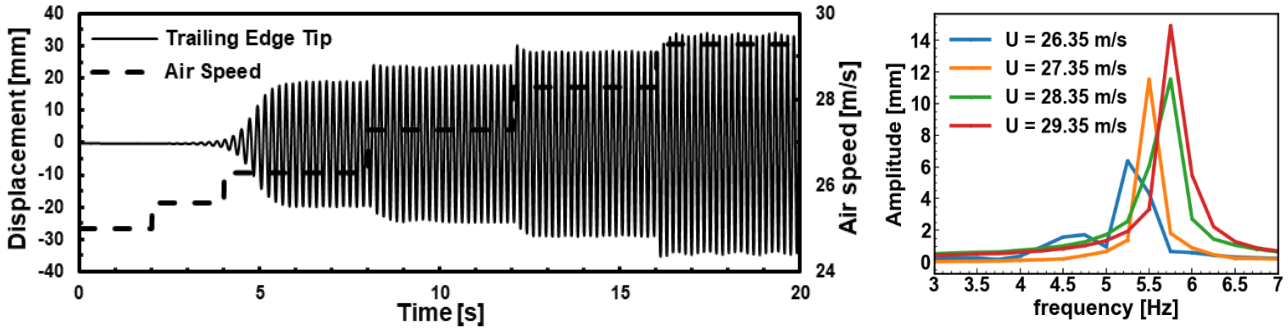

Figure 15: Simulation 4, step size 0.01 [s] and 10 iterations

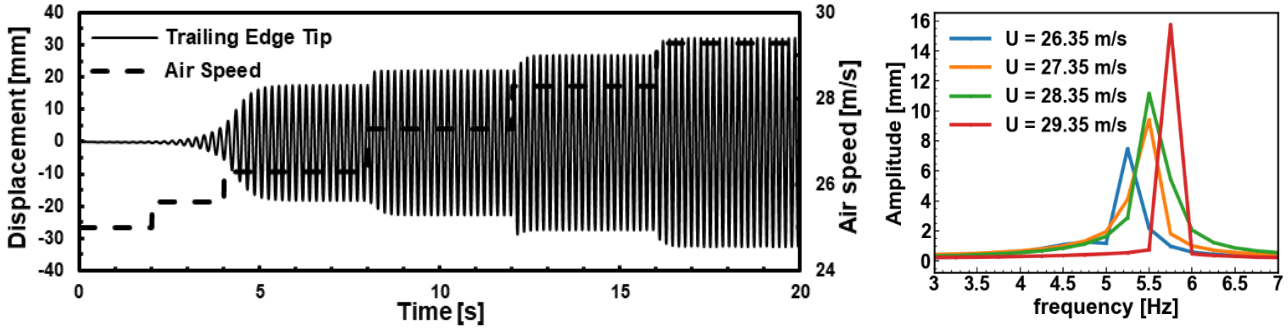

Figure 16: Simulation 5, step size 0.005 [s] and 5 iterations

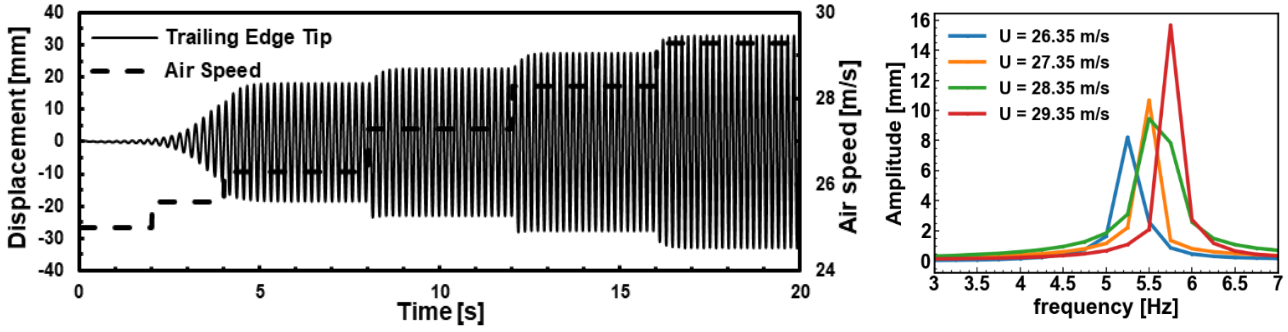

Figure 17: Simulation 6, step size 0.005 [s] and 10 iterations

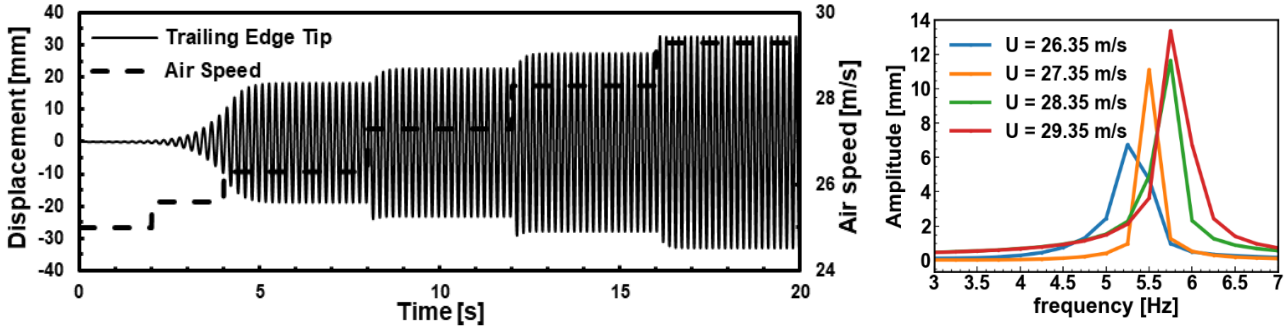

Figure 18: Simulation 7, step size 0.002 [s] and 5 iterations

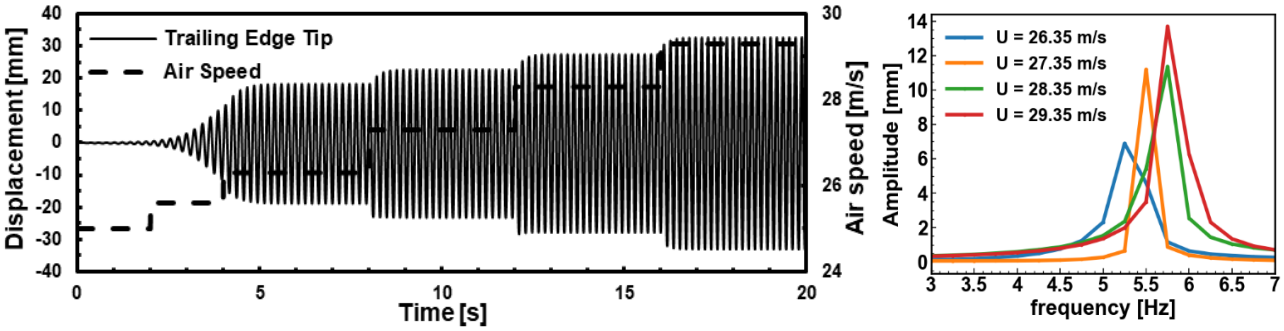

Figure 19: Simulation 8, step size 0.002 [s] and 10 iterations

The observations from plateau peak fluctuation, time-to-LCO, first-LCO plateau amplitude, and the dominant frequency indicate that Δt = 0.005 s provides the best balance between numerical stability and computational cost for the present model. The Δt = 0.002 s simulations offer only marginal changes in time-to-LCO and do not reduce plateau scatter relative to Δt = 0.005 s, while incurring a large computational penalty. Meanwhile, Δt = 0.02 s is too coarse to produce consistent plateau behaviour and yields a distorted transient development, particularly at low iteration counts. Based on these outcomes, the parameters of Simulation 6 (Δt = 0.005 s, 10 iterations) were selected for the subsequent spanwise FGM study, as they achieve stable and repeatable LCO characteristics with a significantly lower computational cost than the smallest time-step cases.

4.2. Effect of spanwise FGM

By applying a spanwise functionally graded material, the mass-stiffness distribution along the span of the wing is completely changed, thus changing the natural frequencies of the wing. This highly impacts the vibration response of the wing, as we will see later.

Since the material used for validation of the baseline model was Aluminum, it seemed fitting to use Aluminum as the metal component of the FGM. Therefore, the selected components of the functionally graded material of the wing are Aluminum (same properties) for the metal, and Alumina (Al_2O_3) for the ceramic, having the properties in Table 4.

Table 4: Properties of the FGM components

Material	E $[GPa]$	ρ $[kg/m^3]$	ν
Aluminum	70	2700	0.3
Alumina (Al_2O_3)	380	3960	0.3

The wing is made into ten equal-length segments, and the power law distribution presented by [39, 40] is used to find the material properties of the segments. The subscripts (L and R) are left and right, respectively; left is the root of the wing, where the Aluminum (metal) is at the highest concentration (Figure 20).

$$P(z) = (P_L - P_R)\left(1 - \frac{x}{L}\right)^k + P_R \qquad (9)$$

Where $P(z)$ is the material property of the segment, calculated using the spanwise location of the segment's center x, P_L and L are the properties of Aluminum and Alumina (Al_2O_3), respectively. L is the span of the wing, K is the power law index that determines the material composition profile along the span of the wing. In this study, three cases of spanwise material grading from left to right are used: k = 0.5, k = 1, and k = 2.

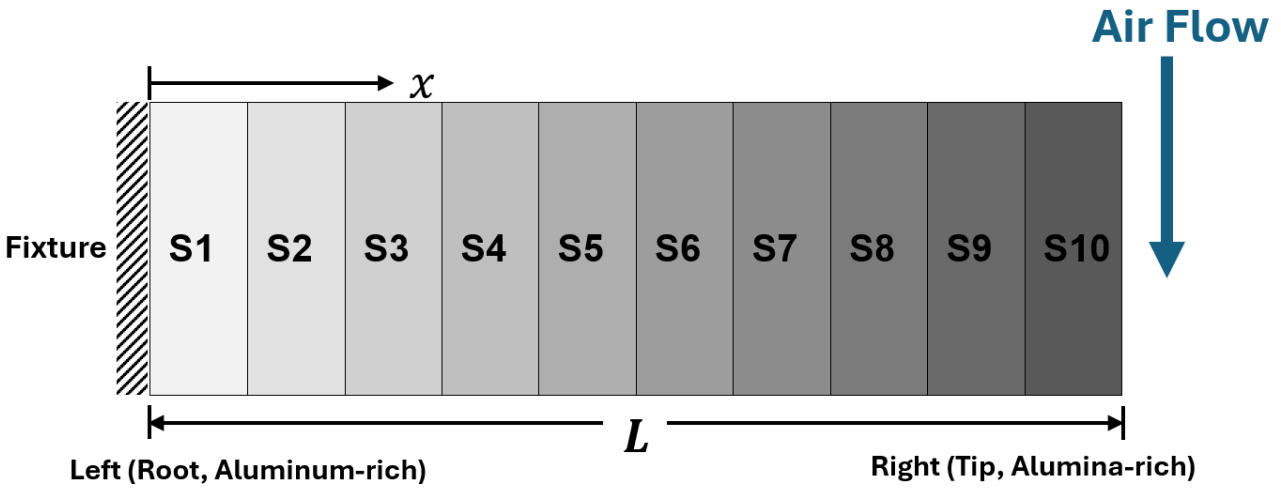

Figure 20: Illustration of the segmented wing

Following the setup as described above, the properties of each segment are presented in Table 5.

Table 5: Material properties of the segments, where the units are *GPa* for *E*, and $\left(kg/m^3\right)$ for ρ. The values are calculated using Error! Reference source not found.**) and rounded for presentation in the table.**

Index k	Property	Segments									
		1	2	3	4	5	6	7	8	9	10
1	E	85.50	116.50	147.50	178.50	209.50	240.50	271.50	302.50	333.50	364.50
	ρ	2763	2889	3015	3141	3267	3393	3519	3645	3771	3897
0.5	E	77.85	94.19	111.53	130.07	150.10	172.05	196.60	225.00	259.94	310.68
	ρ	2732	2798	2869	2944	3026	3115	3215	3330	3472	3678
2	E	100.23	156.03	205.63	249.03	286.23	317.23	342.03	360.63	373.03	379.23
	ρ	2823	3050	3251	3428	3579	3705	3806	3881	3932	3957

Other than the segmentation and material properties, the setup of the FGM FSI model is identical to the validated baseline simulation 6 in the time step study (Δt 0.005 s and 10 iterations). This is to ensure that the results of this simulation are different only due to the application of the discretized FGM. The response of the spanwise-graded Al/Al_2O_3 wing is compared with the results of simulation 6. The material grading increases the stiffness and mass towards the wing tip; intuitively, the effects of the increased stiffness and increased mass contradict each other. The increased stiffness raises the natural frequency, while the increase in tip inertia due to mass increase lowers it. Figure 21 shows the response of the linearly graded wing trailing edge tip; no flutter is observed over the simulated velocity profile, therefore, the net effect is in favor of the increased stiffness, Table 6 shows the natural frequencies of the first two modes for each model, mode 1 is bending, and mode 2 is torsional. The tip response does not exhibit the exponential growth that characterizes instability; shifts in the amplitudes are observed when the air speed changes, the shifts are less pronounced when the air speed is more than the critical speed.

Table 6: Modal frequencies (in Hz) of the baseline and FGM models

Model	Mode 1	Mode 2
Baseline	1.492	7.692
FGM k=0.5	1.567	9.373
FGM k=1	1.657	10.245
FGM k=2	1.819	11.395

While the dominant frequencies of the baseline model lie between 5–6 Hz for air speeds above the critical value (Figure 17), the dominant frequencies of the linearly graded FGM model shift upward into the 6–9 Hz range and become less orderly compared to the cleaner baseline spectrum; a small spike in the 31–33 Hz range is also

observed for the FGM model. For the baseline wing, the first two natural frequencies are 1.492 and 7.692 Hz, whereas for the FGM cases, they increase with grading index, reaching 1.819 and 11.395 Hz for k = 2. This upward shift indicates that the graded material distribution increases the effective stiffness-to-mass ratio and therefore elevates the higher-mode frequency bands. Consequently, the dominant response components of the FGM wing moving from the 5–6 Hz range toward higher bands are consistent with a change in the relative contribution of the modes to the measured response. Moreover, the response of the FGM wing shows very small amplitudes, Figure 22 shows the tip displacement RMS against air speed. The RMS displacement remains lower than 0.1 mm, and is mainly flat across all tested air speeds; clearly contrasting the results of the baseline, where the RMS increases as air speed increases.

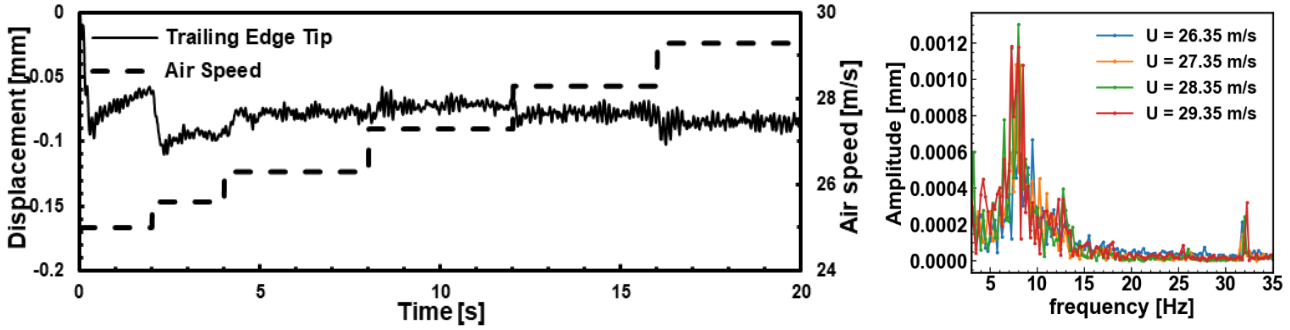

Figure 21: Linear FGM wing trailing edge tip response

For the FGM wing cases with k = 0.5 and k = 2 (Figure 23 & Figure 24), the tip displacement results exhibit similar behavior to the linear grading case, where no flutter is observed for the studied flow speeds (no exponential growth), the amplitudes shift with flow speed stepping (effect diminishes as flow speed increases). The case with k = 2 produced lower amplitudes than the other cases, and k = 0.5 produced the highest amplitudes, Figure 25 shows the tip displacement RMS of the three FGM cases, and Table 7 presents the RMS values of the baeline and FGM models. In terms of the response frequencies , k = 2 shows a further upward shift of dominant frequencies into the 8–11 Hz range, which aligns with the elevated natural frequencies of the corresponding graded structure, and it exhibits a similar spike near 31–33 Hz. In contrast, for k = 0.5 the dominant frequency band shifts back toward 5–7 Hz, and the spike above 30 Hz is not observed, indicating that both the response frequencies are sensitive to the grading index.

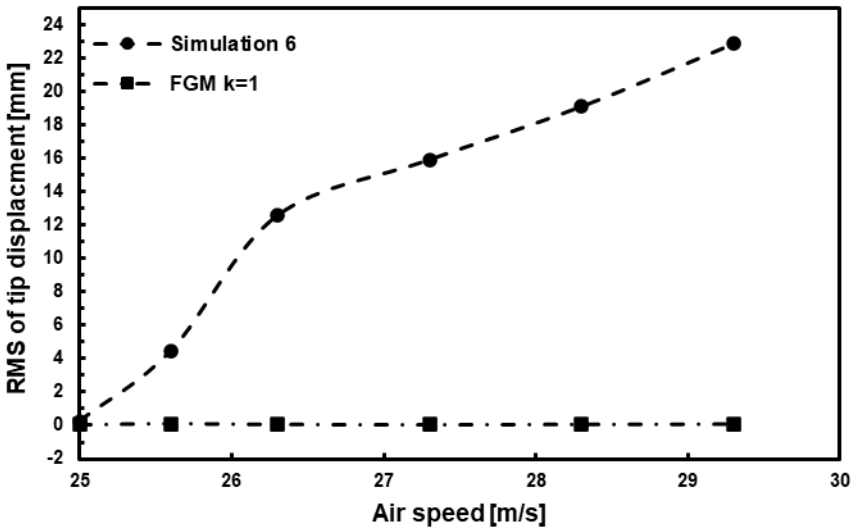

Figure 22: RMS of the trailing edge tip responses of simulation 6 and the linear FGM wing

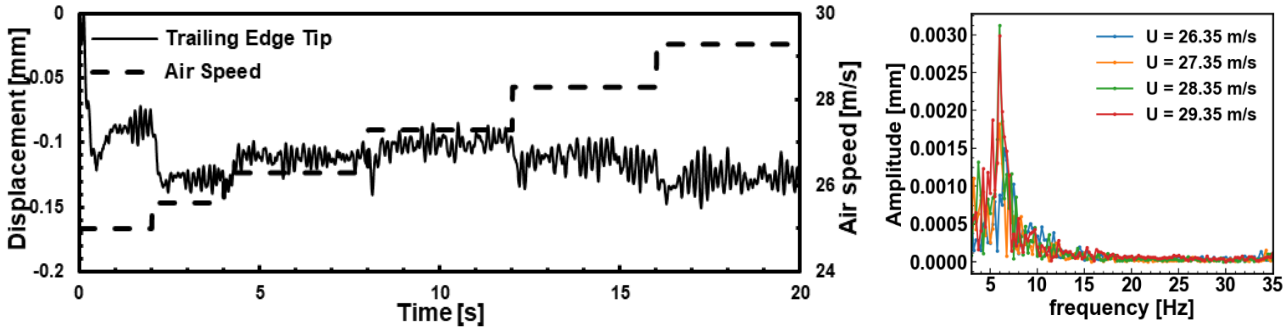

Figure 23: FGM wing (k = 0.5) trailing edge tip response

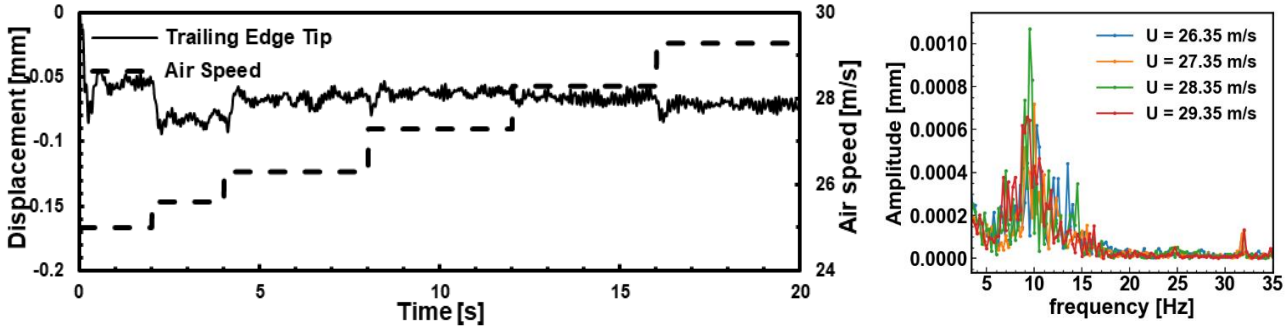

Figure 24: FGM wing (k = 2) trailing edge tip response

Due to the presence of flutter in the baseline model, the stress distributions follow patterns based on the deformation of the wing. There are mainly two locations where maximum Von Mises stresses occur, at the leading edge near the root of the wing, accompanied by elevated stress values close to the midspan of the leading/trailing edges of the wings upper surface, and concentration around the center of the lower surface (Figure 26 & Figure 27); the second is roughly at the midspan of the trailing edge, with higher stress concentration around the center of the wing's upper surface, and midspan of the leading/trailing edges of the wing's lower surface (Figure 28 & Figure 29).

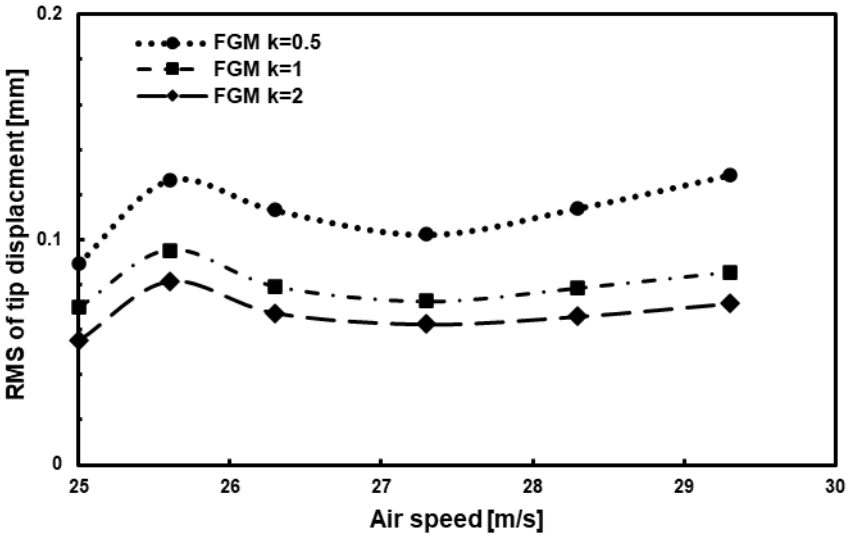

Figure 25: RMS of the trailing edge tip responses for the three FGM cases

Table 7: RMS of the tip displacement for the baseline and FGM cases

Air speed	Baseline	FGM k=1	FGM k=0.5	FGM k=2
25	0.2628	0.0699	0.0893	0.0551
25.6	4.4775	0.0953	0.1264	0.0815
26.35	12.5925	0.0793	0.1131	0.0674
27.35	15.9494	0.0727	0.1023	0.0624
28.35	19.1356	0.0785	0.1140	0.0659
29.35	22.9032	0.0855	0.1287	0.0716

By applying FGM to the wing, the stress distribution over the wing changes as a consequence of the spanwise stiffness change. Figure 30 – Figure 32 show the Von Mises stress distribution at t = 18.575 s for the FGM cases. Contrary to the baseline model, no patterns are observed in the FGM cases, as the wing's response is more random/chaotic. The stress is concentrated near the root at the wing's leading and trailing edges in the FGM cases. For k = 0.5, the maximum Von Mises stress occurred at 17.345 s with a value of 117,350 Pa; at 16.31 s with 98,846 Pa for the linear grading; and at 18.86 s with 102,030 for k = 2. The Von Mises RMS vs flow speed in Figure 33 shows that the k = 0.5 grading produced the highest stress values across all flow speeds, while the linear grading (k = 1) produced the lowest stress values across all flow speeds.

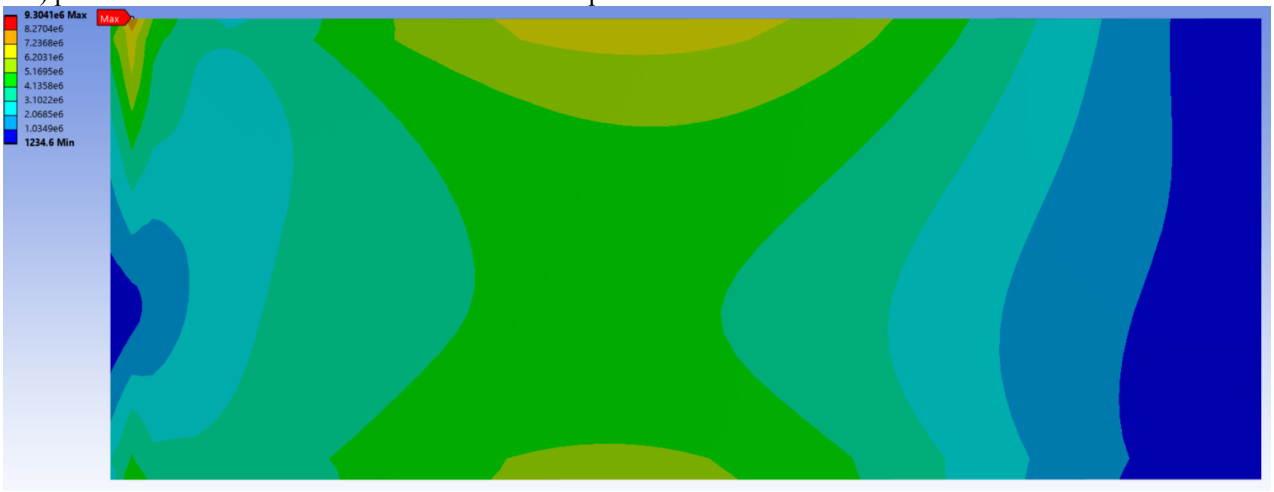

Figure 26: Baseline Von Mises stress (Pa) at 18.5 s upper surface

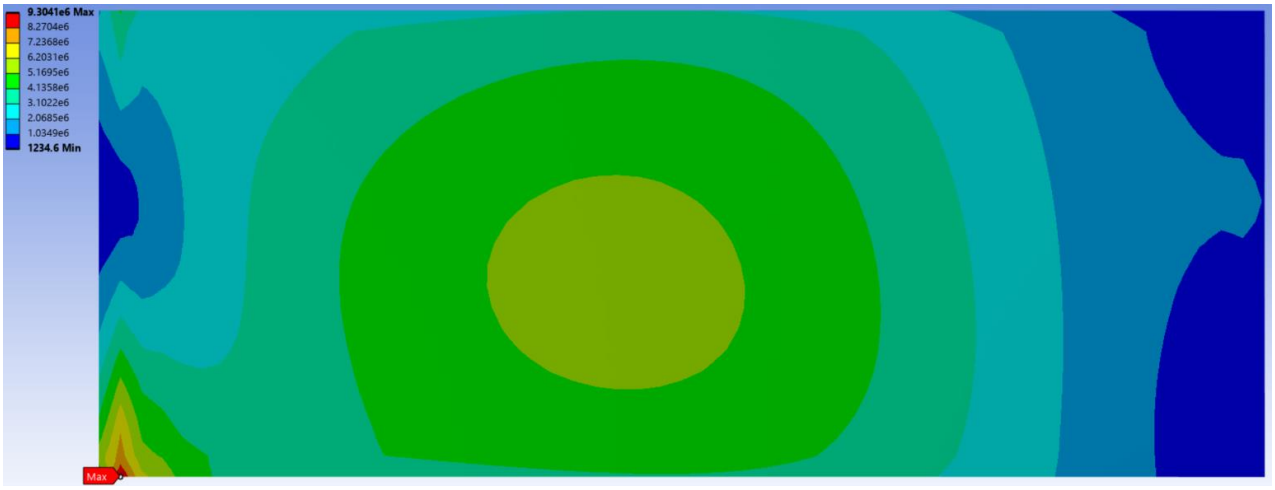

Figure 27: Baseline Von Mises stress (Pa) at 18.5 s lower surface

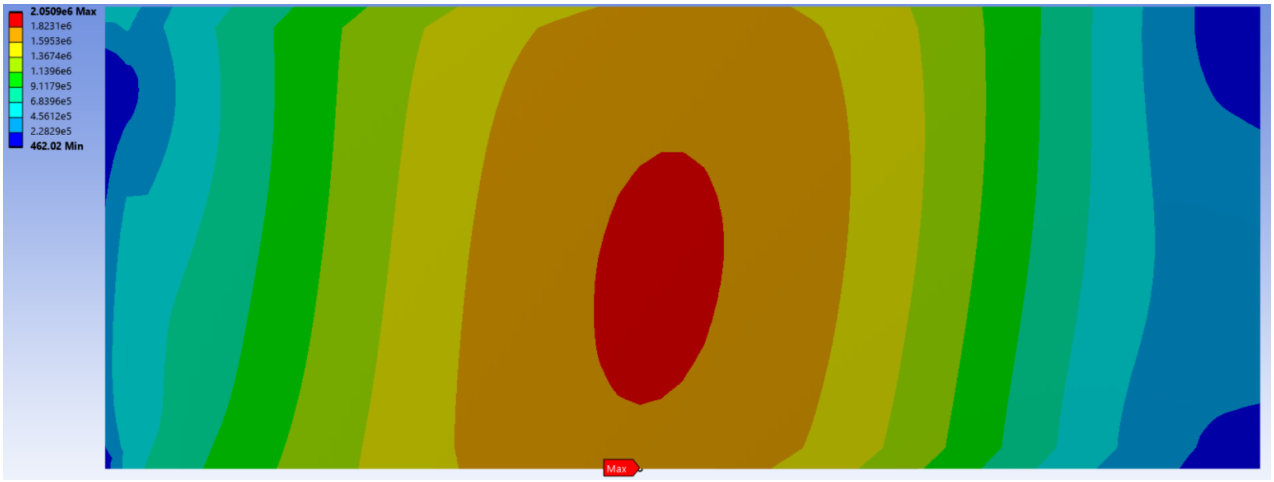

Figure 28: Baseline Von Mises stress (Pa) at 18.575 s upper surface

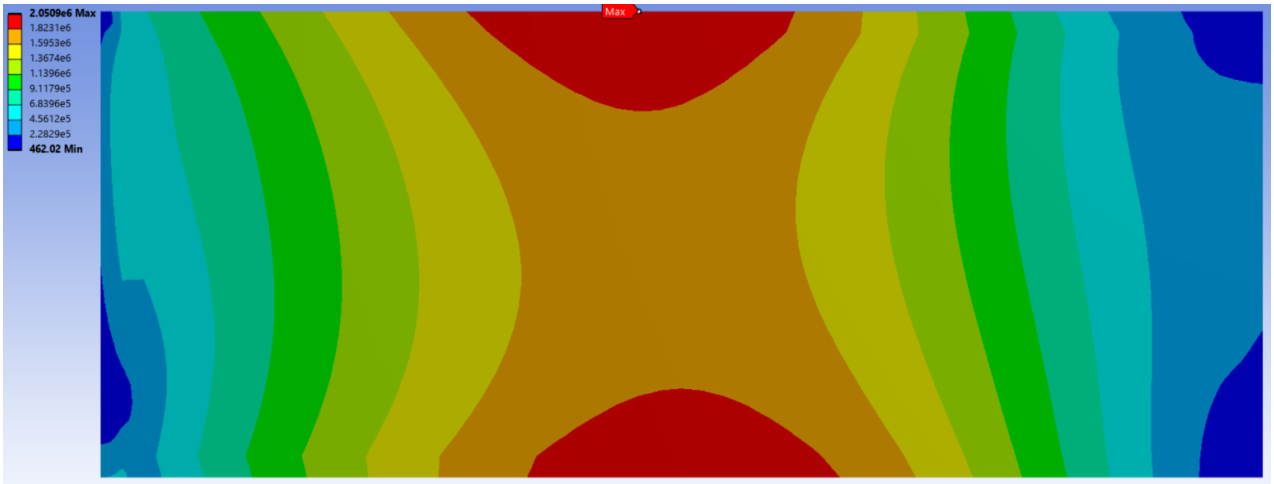

Figure 29: Baseline Von Mises stress (Pa) at 18.575 s lower surface

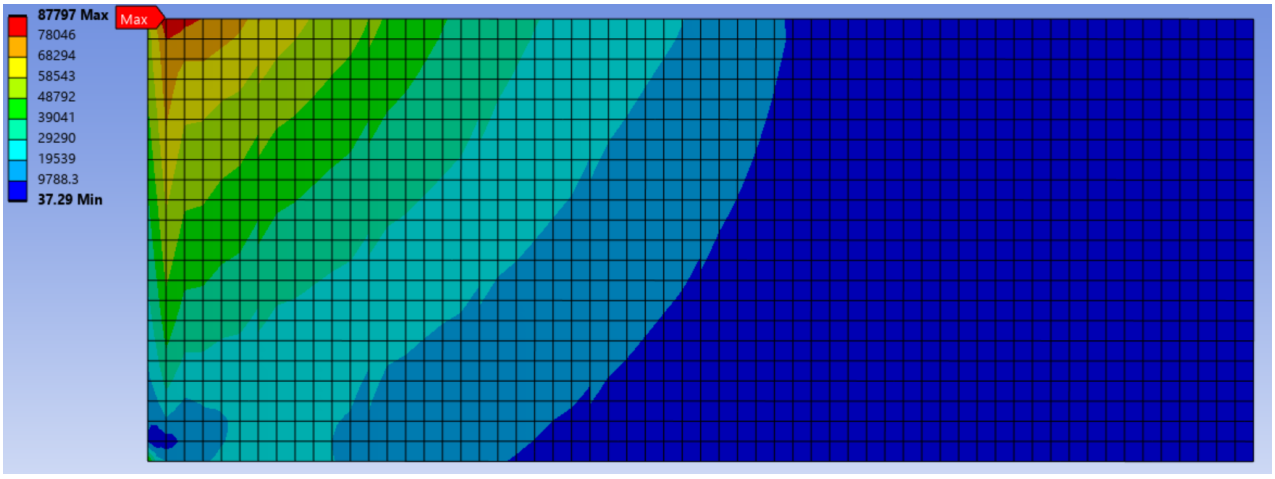

Figure 30: FGM k = 0.5 Von Mises stress (Pa) at 18.575 s upper surface

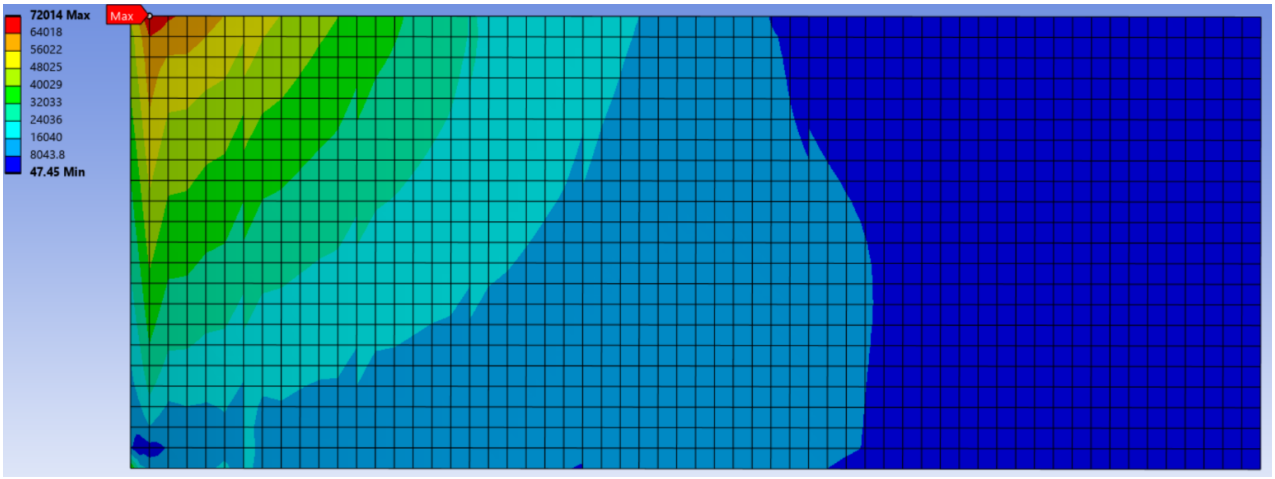

Figure 31: FGM k = 1 Von Mises stress (Pa) at 18.575 s upper surface

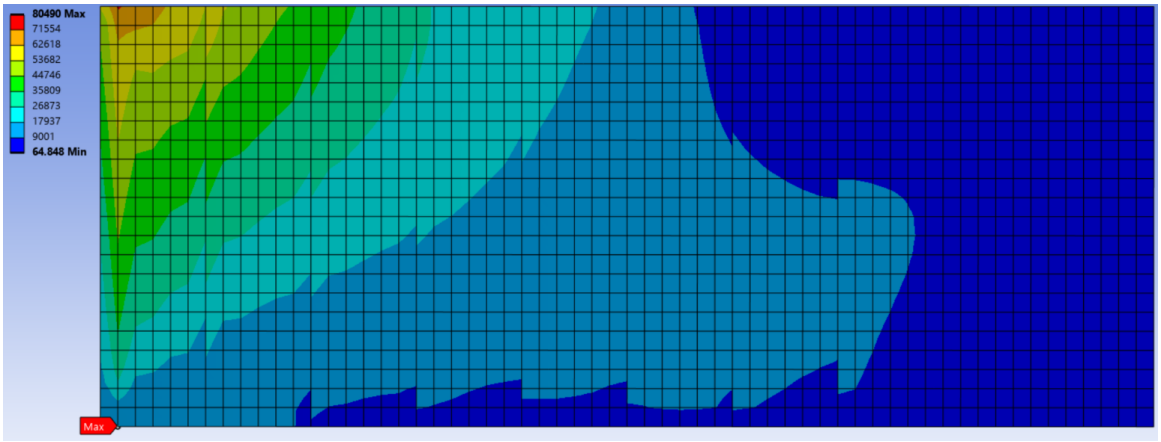

Figure 32: FGM k = 2 Von Mises stress (Pa) at 18.575 s upper surface

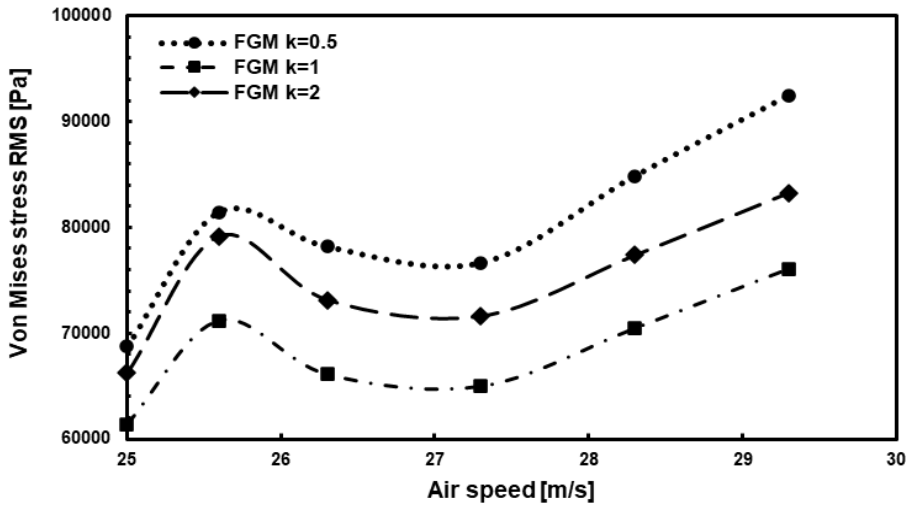

Figure 33: Von Mises stress RMS for the FGM cases

Table 8: Von Mises stress RMS for the baseline and FGM cases

Air speed	Baseline	FGM k=1	FGM k=0.5	FGM k=2
25	158108	61424	68743	66231

25.6	2690006	71182	81458	79192
26.35	8668642	66098	78179	73150
27.35	11289498	64973	76659	71631
28.35	13907986	70461	84882	77383
29.35	17163197	76066	92483	83278

The results indicate that the application of spanwise FGM shifted the flutter boundary above the investigated speed range; the stiffness redistribution has increased the margin sufficiently so that the onset was not reached for the air speed profile used. Because the setup, meshing, and solver controls match the baseline model, the outcome can reasonably be attributed to the spanwise application of FGM.

5. Conclusion

A two-way coupled analysis of an FEA-CFD model is carried out on a simple cantilevered un-swept plate modeled as a wing with an aspect ratio of 2.5 and a chord length of 0.425 m. The fluid-structure interaction model is presented to study the sensitivity of the flutter prediction to the time step size and number of coupling iterations across eight runs. Then, selecting the most computationally cost-efficient settings (without compromising the accuracy of the results) to study the effect of applying an Al/Al_2O_3 spanwise FGM, the wing is split into ten spanwise segments, and the material is graded using three different grading indices. The main observations of these studies are:

- Coarse step sizes delay LCO development.
- Decreasing the time step size reduced the oscillation's peak to peak fluctuations.
- As step sizes decrease, the model's sensitivity to the number of iterations decreases.
- Setting Δt 0.005 s and 10 iterations yielded results nearly indistinguishable from the finest runs at a much lower computational cost and, therefore, recommended for reproducible flutter simulations of this configuration.
- The FGM wing remained free of flutter for all tested air speeds, showing small trailing edge tip motion; therefore, it is inferred that the mass-stiffness re-distribution has shifted the flutter boundary beyond the investigated air flow profile.
- The stiffness re-distribution over the wing and the lack of flutter in the FGM models caused the stress concentration to shift mainly to the leading edge of the wing near the root.

Overall, spanwise linear grading provides a stabilizing effect in the present model, while the recommended numerical controls balance fidelity and cost under license limitations.

References

[1] J.-P. Song, G.-L. She, M. Eltaher, Nonlinear aero-thermo-elastic flutter analysis of stiffened graphene platelets reinforced metal foams plates with initial geometric imperfection, *Aerospace Science and Technology,* Vol. 147, pp. 109050, 2024.

[2] D. H. Hodges, G. A. Pierce, 2011, *Introduction to Structural Dynamics and Aeroelasticity*, Cambridge University Press, Cambridge, 2ed.

[3] F. Liu, J. Cai, Y. Zhu, H. Tsai, A. Wong, Calculation of wing flutter by a coupled fluid-structure method, *Journal of aircraft,* Vol. 38, No. 2, pp. 334-342, 2001.

[4] X. Chen, G.-C. Zha, M.-T. Yang, Numerical simulation of 3-D wing flutter with fully coupled fluid–structural interaction, *Computers & fluids,* Vol. 36, No. 5, pp. 856-867, 2007.

[5] C. Bibin, M. J. Selvaraj, S. Sanju, Flutter analysing over an aircraft wing during cruise speed, *Procedia Engineering,* Vol. 38, pp. 1950-1961, 2012.

[6] R. F. Latif, M. Khan, A. Javed, S. Shah, S. Rizvi, A semi-analytical approach for flutter analysis of a high-aspect-ratio wing, *The Aeronautical Journal,* Vol. 125, No. 1284, pp. 410-429, 2021.

[7] J. Liu, Y. Zhang, Y. Zhang, S. Kitipornchai, J. Yang, Aeroelastic analyses of functionally graded aluminium composite plates reinforced with graphene nanoplatelets under fluid-structural interaction, *Aerospace Science and Technology,* Vol. 136, pp. 108254, 2023.

[8] G. Wenzhi, S. Yongtao, N. Lu, C. Gang, Fluid-structure interaction simulation for multi-body flexible morphing structures, *Chinese Journal of Aeronautics,* Vol. 37, No. 2, pp. 137-147, 2024.

[9] M. Furquan, S. Mittal, A finite element framework for fluid–membrane interactions involving fracture, *Computer Methods in Applied Mechanics and Engineering,* Vol. 417, pp. 116438, 2023.

[10] S. Tiomkin, D. E. Raveh, A review of membrane-wing aeroelasticity, *Progress in Aerospace Sciences,* Vol. 126, pp. 100738, 2021.
[11] J. Valášek, P. Sváček, On aerodynamic force computation in fluid–structure interaction problems—Comparison of different approaches, *Journal of Computational and Applied Mathematics,* Vol. 429, pp. 115208, 2023.
[12] P. Sváček, On numerical simulation of fluid-structure interaction problems using variational multiscale methods, *Journal of Computational and Applied Mathematics,* Vol. 427, pp. 115125, 2023.
[13] N. Tsushima, K. Saitoh, K. Nakakita, Structural and aeroelastic characteristics of wing model for transonic flutter wind tunnel test fabricated by additive manufacturing with AlSi10Mg alloys, *Aerospace Science and Technology,* Vol. 140, pp. 108476, 2023.
[14] Y. Liu, W. Ma, Nonlinear oscillations of a composite stepped piezoelectric cantilever plate with aerodynamic force and external excitation, *Mathematics,* Vol. 11, No. 13, pp. 3034, 2023.
[15] H. I. Abdoulaye, R. El Maani, Numerical Simulation of Fluid–Structure Interaction in Wind Turbines: A Reduced-Order Approach via Periodic Modeling and Substructuring, *Applied Mechanics,* Vol. 7, No. 1, pp. 1, 2025.
[16] J. Knight, S. Fels, B. Beazley, G. Haritos, A. Lewis, Fluid–structure interaction of symmetrical and cambered spring-mounted wings using various spring preloads and pivot point locations, *Applied Mechanics,* Vol. 2, No. 3, pp. 591-612, 2021.
[17] X. P. Hadebe, B. X. Tchomeni Kouejou, A. A. Alugongo, D. F. Sozinando, Comparative Structural and Hydraulic Assessment of a DN3000 Double Eccentric Butterfly Valve Blade Using a Coupled CFD–FEM Approach, *Applied Mechanics,* Vol. 7, No. 1, pp. 7, 2026.
[18] W. Wang, W. Qian, Y. Bai, K. Wang, Numerical studies on the thermal-fluid-structure coupling analysis method of hypersonic flight vehicle, *Thermal science and engineering progress,* Vol. 40, pp. 101792, 2023.
[19] K. Dhital, A. T. Nguyen, J.-H. Han, Aeroelastic modeling and analysis of wings in proximity, *Aerospace Science and Technology,* Vol. 130, pp. 107955, 2022.
[20] Y. Guo, Y. Guo, Y. Zhang, L. Li, D. Zhang, S. Chen, M. A. Eltaher, Thermally induced vibration of a flexible plate with enhanced active constrained layer damping, *Aerospace,* Vol. 11, No. 7, pp. 504, 2024.
[21] C. Fan, R. A. Adjei, Z. Ye, J. Cui, Investigation on aeroelastic characteristics of mistuned low-speed axial compressor rotor: numerical methodology and optimization, *Aerospace Science and Technology,* Vol. 143, pp. 108735, 2023.
[22] Y.-W. Zhang, G.-L. She, M. Eltaher, Nonlinear transient response of graphene platelets reinforced metal foams annular plate considering rotating motion and initial geometric imperfection, *Aerospace Science and Technology,* Vol. 142, pp. 108693, 2023.
[23] Y. Li, J. Xie, F. Wang, Y. Li, Shear Lag Effect of Ultra-Wide Box Girder under Influence of Shear Deformation, *Applied Sciences,* Vol. 14, No. 11, pp. 4778, 2024.
[24] D. Zhang, Z. Liu, W. Li, J. Zhang, L. Cheng, G. Hu, Fluid-structure interaction analysis of wind turbine aerodynamic loads and aeroelastic responses considering blade and tower flexibility, *Engineering Structures,* Vol. 301, pp. 117289, 2024.
[25] Z. Li, Z. Gao, Y. Dai, C. Wen, L. Zhang, J. Wang, Unsteady aeroelastic performance analysis for large-scale megawatt wind turbines based on a novel aeroelastic coupling model, *Renewable Energy,* Vol. 218, pp. 119370, 2023.
[26] G. Frulla, G. Parente, Design Considerations for a Compressed Stiffened Plate with Skin–Stringer Debonding Based on the Evaluation of Adhesive Layer Stress Distribution, *Applied Mechanics,* Vol. 6, No. 1, pp. 7, 2025.
[27] R. Mahmoudi, M. Hosseini, A. Soleimani, Stability analysis of conveying-nanofluid functionally graded nanotube based on nonlocal couple stress theory, *Journal of Computational Applied Mechanics,* Vol. 54, No. 2, pp. 309-322, 2023.
[28] A. H. Kherief Nacereddine, O. Kholai, M. Chekired, M. Kadja, T. H. Mai, Numerical Simulation of Laminar Flow of a Non-Newtonian Bentonite Solution in a Horizontal Pipe, *Journal of Computational Applied Mechanics,* Vol. 55, No. 4, pp. 552-566, 2024.
[29] S. B. Pope, Turbulent flows, *Measurement Science and Technology,* Vol. 12, No. 11, pp. 2020-2021, 2001.
[30] F. R. Menter, Two-equation eddy-viscosity turbulence models for engineering applications, *AIAA journal,* Vol. 32, No. 8, pp. 1598-1605, 1994.
[31] K. Bathe, E. Wilson, Stability and accuracy analysis of direct integration methods, *Earthquake Engineering & Structural Dynamics,* Vol. 1, No. 3, pp. 283-291, 1972.
[32] K.-J. Bathe, Finite element procedures prentice-hall, *New Jersey,* Vol. 1037, No. 1, pp. 1-6, 1996.

[33] N. M. Newmark, A method of computation for structural dynamics, *Journal of the engineering mechanics division,* Vol. 85, No. 3, pp. 67-94, 1959.
[34] B. Arrondeau, Z. A. Rana, Computational aerodynamics analysis of non-symmetric multi-element wing in ground effect with humpback whale flipper tubercles, *Fluids,* Vol. 5, No. 4, pp. 247, 2020.
[35] P. H. Oosthuizen, W. E. Carscallen, 2013, *Introduction to compressible fluid flow*, CRC press,
[36] H. Qansh, *Aerodynamic Analysis on Modified Horizontal-Axis-Wind-Turbine*, Thesis, University of Sheffield, 2022.
[37] H.-Y. Xu, C.-L. Qiao, H.-Q. Yang, Z.-Y. Ye, Delayed detached eddy simulation of the wind turbine airfoil S809 for angles of attack up to 90 degrees, *Energy,* Vol. 118, pp. 1090-1109, 2017.
[38] C. P. Butterfield, G. Scott, W. Musial, Comparison of wind tunnel airfoil performance data with wind turbine blade data, 1992.
[39] H. H. Patil, J. Pitchaimani, M. Eltaher, Buckling and vibration of beams using Ritz method: effects of axial grading of GPL and axially varying load, *Mechanics of Advanced Materials and Structures,* Vol. 31, No. 16, pp. 3861-3874, 2024.
[40] A. E. Alshorbagy, M. A. Eltaher, F. Mahmoud, Free vibration characteristics of a functionally graded beam by finite element method, *Applied mathematical modelling,* Vol. 35, No. 1, pp. 412-425, 2011.